ChemComm

COMMUNICATION

View Article Online
View Journal | View Issue

Cite this: *Chem. Commun.*, 2024, **60**, 13698

Received 30th September 2024,
Accepted 24th October 2024

DOI: 10.1039/d4cc05029k

rsc.li/chemcomm

TEMPO-oxidized cellulose nanofiber hydrogel electrolyte for rechargeable Zn-ion batteries†

Kento Kimura, [ab] Vittorio Marangon, [cd] Taiga Fukuda, [e] Mana Suzuki, [e] Nantapat Soontornnon, [e] Yoichi Tominaga *[abe] and Jusef Hassoun *[bcd]

A hydrogel composed of TEMPO-oxidized cellulose and zinc perchlorate is proposed as an electrolyte for rechargeable Zn-ion battery. The non-flowable solid-like electrolyte has strong shear-thinning behavior, room temperature conductivity of $\sim 10^{-1}$ S cm^{-1}, and stable Zn/electrolyte interphase. The Zn-ion gel-battery with a β-MnO_2 cathode delivers over 100 mA h g^{-1} at 1.5 V allowing safe energy storage.

Zinc batteries have attracted attention as energy storage devices due to high safety, abundance of raw material resources, and environmental friendliness.[1,2] Zinc is safer than Li and Na due to low reactivity, and has low toxicity, limited cost, and a theoretical specific capacity of 820 mA h g^{-1}. The potential of −0.76 V *vs.* standard hydrogen electrode (SHE) allows the implementation of aqueous electrolytes for Zn batteries without hydrogen evolution at basic pH.[3] Alkaline zinc batteries are commercialized as a non-rechargeable primary system.[4] This configuration limits the applicability of the battery for energy storage, which requires instead a rechargeable version of the cathode and anode.[5] MnO_2 revealed electrochemical activity in aqueous media with reversible formation of manganese mixed oxides through ion exchange and phase changes between 0.8 and 1.8 V *vs.* Zn^{2+}/Zn.[6] Instead, Zn was limited by hydrogen evolution in acidic conditions, and relevant dendrite growth, unless a stable solid electrolyte interphase (SEI) was formed.[4] Solidified hydrogel electrolytes can prevent electrolyte leakage and suppress dendrite formation on Zn due to their elasticity.[7,8] Gelled electrolytes revealed the consolidation of a stable interphase with robust SEI, even in an acid environment.[9] We report a hydrogel based on TEMPO-oxidized 2,2,6,6-tetramethylpiperidine-1-oxyl cellulose nanofiber (TOCNF) as an electrolyte matrix for rechargeable Zn batteries. The TEMPO oxidation chemical fibrillation method is an efficient technique to fabricate cellulose nanofibers.[10–12] Accordingly, uniform cellulose nanofibers (CNFs) of ∼3 nm width can be obtained by introducing sodiated carboxyl groups at high density into cellulose raw material to prepare a hydrogel framework. Thus, the TOCNF hydrogel dissolving $Zn(ClO_4)_2$ salt is exploited for rechargeable Zn-ion batteries with promising properties.

The conductivity at 25 °C of this electrolyte, as well as the rheological features and the Fourier-transform infrared (FT-IR) spectra of the hydrogel with and without the conducting salt are displayed in Fig. 1. The ionic conductivity is evaluated by electrochemical impedance spectroscopy (EIS) in Fig. 1a. The non-linear least squares (NLLS) analysis allows the estimation of the electrolyte resistance (R_e) through the R_eQ equivalent circuit,[13,14] leading to ionic conductivity of 2.9×10^{-1} S cm^{-1}. Although the TOCNF hydrogel electrolyte appears like a non-stretchable opalescent solid-like gel (photographic inset of Fig. 1a), its conductivity value is slightly exceeding that of the reference aqueous solutions containing $Zn(ClO_4)_2$ at 25 °C (*i.e.*, 1.8×10^{-1} S cm^{-1} as determined by the Nyquist plot of Fig. S1 in ESI†). This outcome can be attributed to the relevant water uptake of the membrane allowed by the gelation ability of the TOCNF (see the sample's composition in Table S1 and Experimental details in the ESI†),[15] and to a slightly higher acidity of the gel electrolyte (pH ∼3.7) compared with the reference solution (pH ∼4.5). The H^+ can increase the ionic conductivity of the jellified electrolyte matrix by involving the proton-hopping into the Grotthuss mechanism, throughout hydrogen bonds with fixed H_2O.[16] The slight acidity of the electrolyte can in principle promote the reversibility of both Zn and MnO_2 redox reactions, as long as a stable SEI layer is formed at the electrode surface.[9] Fig. 1b shows the flow curve of

[a] *Department of Applied Chemistry, Graduate School of Engineering, Tokyo University of Agriculture and Technology, 2-24-16, Naka-cho, Koganei-Shi, Tokyo 184-8588, Japan. E-mail: ytominag@cc.tuat.ac.jp*
[b] *Institute of Global Innovation Research (GIR), Tokyo University of Agriculture and Technology, 2-24-16, Naka-cho, Koganei-Shi, Tokyo 184-8588, Japan*
[c] *Department of Chemical, Pharmaceutical and Agricultural Sciences, University of Ferrara, Via Fossato di Mortara 17, 44121, Ferrara, Italy. E-mail: jusef.hassoun@unife.it*
[d] *Graphene Lab, Istituto Italiano di Tecnologia, Via Morego 30, Genoa 16163, Italy*
[e] *Graduate School of Bio-Applications and Systems Engineering (BASE), Tokyo University of Agriculture and Technology, 2-24-16, Naka-cho, Koganei-Shi, Tokyo 184-8588, Japan*

† Electronic supplementary information (ESI) available. See DOI: https://doi.org/10.1039/d4cc05029k

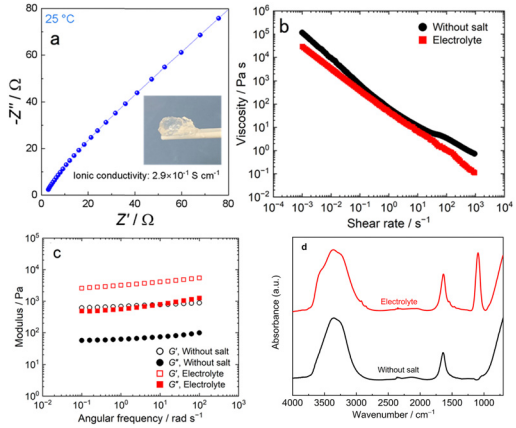

Fig. 1 (a) Nyquist plot of the TOCNF hydrogel electrolyte at 25 °C (frequency: 1 kHz–100 Hz; voltage signal: 10 mV), and photographic image in the inset. (b) Flow curves and (c) frequency dependences of storage modulus (G') on loss modulus (G'') of the TOCNF hydrogel with and without $Zn(ClO_4)_2$ at 25 °C. (d) FT-IR spectra of the TOCNF hydrogel with and without $Zn(ClO_4)_2$.

the TOCNF hydrogel electrolyte and of the hydrogel without any salt for comparison. A notable shear-thinning behavior is confirmed in the flow curve of the electrolyte, with a viscosity ranging over five orders of magnitude for the measurement interval of the shear rate. In this regard, the viscosity of the hydrogel electrolyte is observed to be slightly lower than that of the salt-free hydrogel. The above strong shear-thinning behavior is a favorable characteristic since a high viscosity at low shear rate enhances the storage stability, while low viscosity at high shear rate may facilitate manufacturing by coating or spraying. A comparison between flow curves for the hydrogel electrolyte and the salt-free hydrogel, including the measurement step under increasing shear rate, is shown in Fig. S2 in the ESI.† The curves for both hydrogels show response peaks in the low shear rate region under increasing shear rate conditions, and hysteresis in response to increasing and decreasing shear rate. Peaks and hysteresis can be attributed to the yielding and thixotropic nature of the TOCNF hydrogel, respectively. The absence of a significant modification of the flow curves suggests that the salt addition doesn't affect the stability of the hydrogel, which is a favorable outcome for promoting electrolyte applications. Additional insights are given in Fig. 1c, which shows the frequency sweep of viscoelasticity measurement. The results support the solid-like nature of the hydrogel, with the storage modulus exceeding the loss modulus in the three-digit frequency range.[17] The frequency dependence of the storage and loss moduli of the hydrogel electrolyte exhibits relatively flat trends over the measurement range, in which the moduli trend seems to be higher than that of the salt-free hydrogel. The higher modulus suggests the formation of an internal network structure with physical cross-linking between TOCNF and zinc ions, which improves the mechanical stability of the hydrogel electrolyte.[17] This hypothesis is supported by the results of the strain sweep reported in Fig. S3 in the ESI† showing for the salt-free hydrogel undesired dilatancy behavior, which is suppressed in the electrolyte.

Further insight is given by FT-IR spectra of the TOCNF hydrogel with and without $Zn(ClO_4)_2$ salt in Fig. 1d. The figure reveals for both materials the characteristic wide band at wavenumbers ranging from 3700 to 3100 cm^{-1}, related with the stretching of the –OH bond of water,[18] possibly including the absorption band at 3391 cm^{-1} due to hydroxyl group stretching.[19] The absence in the TOCNF hydrogel without salt (black curve) of the bands at 2906 cm^{-1} and 1373 cm^{-1} ascribed with the stretching of C–H groups of the glucose unit, and of the one at 1061 cm^{-1} assigned to the –C–O– group of secondary alcohols or ethers in the backbone, typically observed in commercial cellulose, accounts for the formation of a water-rich gelled structure rather than a dry-polymer or crystalline one.[19] The salt addition promotes the appearance in the related FT-IR spectrum (red curve) of a band centered at 1100 cm^{-1} ascribed with the ion-bonded ClO_4^- group, thus evidencing the actual retention of the ions.[20]

The compatibility of the hydrogel electrolyte with Zn is investigated in Fig. 2 by EIS of a symmetric cell during aging (Fig. 2a and b) and galvanostatic Zn stripping/plating (Fig. 2c). The Nyquist plots in Fig. 2a are analyzed *via* NLLS fit with the results in Table 1 and Fig. 2b. The table describes the spectra with the $R_e(R_1Q_1)(R_2Q_2)$ equivalent circuit, where the width of the semicircles in the plots is measured through R_1 and R_2, *i.e.*, interphase contributions of charge transfer and SEI ($R_i = R_1 + R_2$).

The NLLS analyses show an initial interphase resistance of ~480 Ω that sharply increases to ~1000 Ω after 1 day, and gradually decreases and stabilizes at ~830 Ω after 5 days (Fig. 2b). This trend suggests the fast formation of a resistive SEI layer, that gradually stabilizes through time with the enhancement of the interphase conductivity. Analogous behavior is deduced from the Zn stripping/plating test in Fig. 2c, with gradual increase of

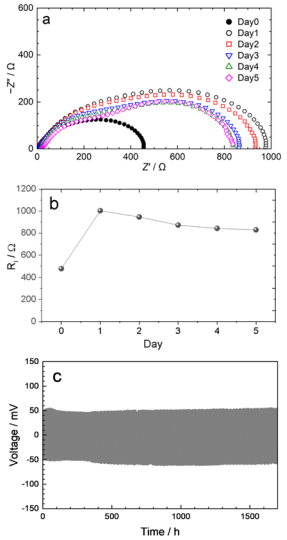

Fig. 2 (a) Nyquist plots over aging of the Zn|Zn symmetric cell with the TOCNF hydrogel electrolyte at 25 °C, and (b) related resistance trend: frequency range: 500 kHz–0.02 Hz; applied signal: 10 mV. (c) Voltage profiles of a galvanostatic plating/stripping test performed at 25 °C on a Zn|Zn symmetric cell at a current density of 0.2 mA cm^{-2} with a step time of 1 h.

Table 1 NLLS analyses on Nyquist plots of Fig. 2a related with EIS on a Zn|Zn cell using TOCNF hydrogel electrolyte over aging

Condition	Circuit	R_1 [Ω]	R_2 [Ω]	R_i [Ω]	χ^2
Assembly	$R_e(R_1Q_1)(R_2Q_2)$	161 ± 19	316 ± 22	477 ± 21	5×10^{-5}
1 day	$R_e(R_1Q_1)(R_2Q_2)$	543 ± 21	461 ± 24	1004 ± 23	5×10^{-5}
2 days	$R_e(R_1Q_1)(R_2Q_2)$	619 ± 27	328 ± 30	947 ± 29	2×10^{-4}
3 days	$R_e(R_1Q_1)(R_2Q_2)$	431 ± 20	442 ± 24	873 ± 22	2×10^{-4}
4 days	$R_e(R_1Q_1)(R_2Q_2)$	359 ± 16	484 ± 20	843 ± 18	2×10^{-4}
5 days	$R_e(R_1Q_1)(R_2Q_2)$	336 ± 15	494 ± 18	830 ± 17	2×10^{-4}

the overpotential to 53 mV during the initial 50 hours, and a subsequent decrease to 48 mV and stabilization to values between 48 and 54 mV held through the whole test exceeding 1500 h. These outcomes confirm the growth of a passivating SEI during the initial stage, which subsequently undergoes stabilization and partial dissolution with a decrease of the electrode/electrolyte interphase resistance.[21]

The SEI on the Zn surface in contact with the TOCNF hydrogel is investigated in Fig. 3 by X-ray photoelectron spectroscopy (XPS) of Zn stored in ambient conditions (*i.e.*, in contact with O_2, N_2, CO_2, H_2O), and after aging for 1 day in contact with the electrolyte (see Experimental section in the ESI† for sample preparation). The XPS of bare Zn ($2p_{3/2}$ signal at 1023 eV, Fig. 3a)[22] suggests the formation at the metal surface by reaction with an atmosphere of –CH bonds (C 1s signal at 285 eV, Fig. 3b),[23] oxygen-containing groups including O–C–O (C 1s signal at 286.5 eV, Fig. 3b),[24] O–C═O (C 1s signal at 288.7 eV, Fig. 3b)[25] and C═O (O 1s signal at 532.5 eV, Fig. 3c),[26] as well as mixed oxides (O 1s signal at 529.5 eV, Fig. 3c).[27] Aging Zn in the electrolyte leads to a decrease of the C–H signal with a concomitant increase of O–C–O, O–C═O (Fig. 3e), and C═O (Fig. 3f) ones, as well as of the mixed oxide one. It is worth mentioning that the unassigned minor peaks in Fig. 3b and e (green, purple) are artifacts resulting from the use of the Gaussian equation for XPS analysis.

Fig. 4 reports the TOCNF hydrogel electrolyte feature in the Zn battery. The electrochemical stability window is determined by linear sweep voltammetry (LSV) in a Zn|graphite cell (Fig. 4a). The anodic scan exhibits a side peak at 1 V *vs.* Zn^{2+}/Zn due to non-oxidized cellulose traces in the electrolyte, justified by the redox potentials of Zn^{2+}/Zn (−0.76 V *vs.* SHE) and cellulose (0.1 to 0.24 V *vs.* SHE),[28] and massive water oxidation at 1.2 V *vs.* SHE (1.9 V *vs.* Zn^{2+}/Zn). The cathodic scan shows slight proton reduction at 0.8 V *vs.* Zn^{2+}/Zn, and Zn plating on graphite at 0 V *vs.* Zn^{+2}/Zn. Hence, the electrolyte stability extends from 0 to 1.8 V *vs.* Zn^{2+}/Zn, which is suitable for rechargeable Zn batteries using MnO_2. The literature indicates for MnO_2 a reaction involving phase transition, with H^+ and Zn^{2+} ion exchange.[6,29–31] The features of the Zn|MnO_2 cell using TOCNF hydrogel electrolyte are evaluated in Fig. 4b by cyclic voltammetry (CV). During the first cathodic scan a main signal below 1.0 V *vs.* Zn^{2+}/Zn is observed, with the shoulder extended until 0.8 V *vs.* Zn^{2+}/Zn. This response reflects reduction of Mn^{4+} to Mn^{3+} in β-MnO_2 with conversion to MnOOH, further reduction to Mn^{2+} with partial dissolution, and Zn^{2+} ion insertion with formation of $Zn(ClO_4)_2$ or hydroxides.[6] The anodic scan shows a single peak at 1.55 V *vs.* Zn^{2+}/Zn coherent with the oxidation of the manganese to Mn^{4+} with deposition of ε-MnO_2 in the electrode.[6] This process includes material rearrangement, also observed for other conversion electrodes as S in Li-cell.[32] The second cathodic scan shows a process at 1.4 V *vs.* Zn^{2+}/Zn due to reduction of ε-MnO_2 to MnOOH, and a second one at 1 V *vs.* Zn^{2+}/Zn due to dissolution of Mn^{2+} with reduction of residual β-MnO_2. The anodic peak splits into a complex one between 1.5 and 1.6 V *vs.* Zn/Zn^{2+} by oxidation of MnOOH and dissolved Mn^{2+} to ε-MnO_2. During the subsequent cycles, the reduction peak at 1 V *vs.* Zn^{2+}/Zn shrinks and the one at 1.4 V grows, while the broad oxidation wave progressively shifts down to 1.5 V *vs.* Zn^{2+}/Zn, as the ε-MnO_2 content increases and the β-MnO_2 one decreases. After cycling, the process stably becomes the reversible oxidation of ε-MnO_2 to MnOOH. The interphase resistance (R_i) is monitored by EIS at the open circuit voltage (OCV) and upon CV (Fig. 4c). The

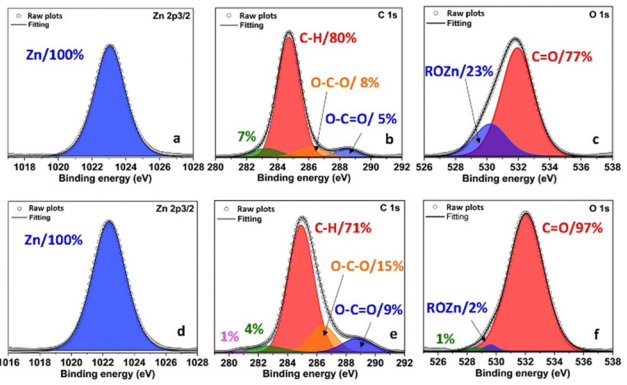

Fig. 3 XPS of the Zn electrode (a)–(c) in the pristine state and (d)–(f) after aging for 1 day with the TOCNF hydrogel electrolyte at 25 °C. Signals of (a) and (d) Zn $2p_{3/2}$, (b) and (e) C 1s, (c) and (f) O 1s.

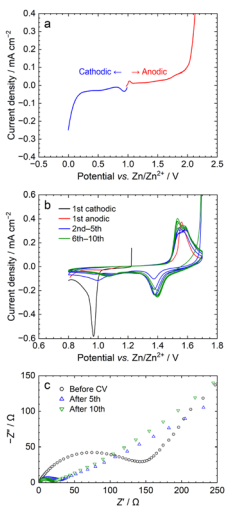

Fig. 4 (a) LSV of the TOCNF hydrogel electrolyte in a Zn|graphite cell, and (b) CV in a Zn|MnO_2 cell between 0.8 and 1.7 V *vs.* Zn^{2+}/Zn. (c) EIS spectra at cell OCV and upon CV at 0.1 mV s^{-1}; frequency range: 500 kHz–0.02 Hz with 10 mV voltage signal.

Table 2 NLLS analyses of EIS spectra reported in Fig. 4 related with measurements performed on the Zn|MnO_2 cell upon CV

Cell condition	Circuit	R_i [Ω]	χ^2
OCV	$R_e(R_iQ_i)Q$	137 ± 1	2×10^{-4}
After 5 cycles	$R_e(R_iQ_i)Q$	18.4 ± 4.2	7×10^{-4}
After 10 cycles	$R_e(R_iQ_i)Q$	15.8 ± 3.1	7×10^{-4}

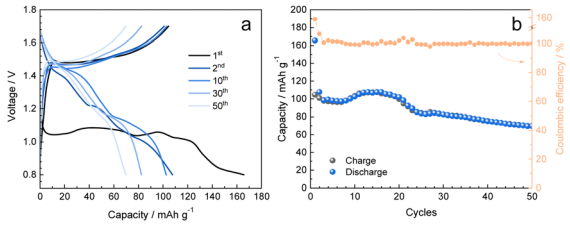

Fig. 5 (a) Galvanostatic voltage profiles and (b) capacity trend with coulombic efficiency of a Zn|MnO_2 cell using the TOCNF hydrogel electrolyte at C/20 rate (1C = 308 mA g^{-1}) between 0.8 and 1.7 V at 25 °C.

NLLS analyses in Table 2 evidence that R_i decreases from 140 Ω to 20 Ω, thus supporting cell enhancement.

Fig. 5 displays the charge/discharge voltage (a) and specific capacity trend (b) upon galvanostatic cycling of a Zn|MnO_2 cell using the TOCNF hydrogel electrolyte at C/20. The first cycle (Fig. 5a) shows discharge above 1.0 V, with fluctuations as the multiple processes described in CV occur, with a specific capacity of 170 mA h g^{-1}. The next charge occurs between 1.5 and 1.7 V, with specific capacity of 105 mA h g^{-1}. The subsequent cycles display the complex two-step discharge, evolving from 1.5 to 1.0 V, and a charge process merged at 1.5 V. The trend in Fig. 5b reveals a maximum capacity of 110 mA h g^{-1}, which fluctuates and stabilizes at 70 mA h g^{-1} over 50 cycles, which is higher than the control cells using a $Zn(ClO_4)_2$ solution (Fig. S4, ESI†), or a thinner gel membrane (Fig. S5) in the ESI.† Despite cells exceeding this performance,[33–38] we originally exploited TEMPO-oxidized CNF hydrogel as a bio-sourced next-generation medium in Zn batteries.

In conclusion, the TEMPO-oxidized CNF hydrogel (Fig. S6 in ESI†) appears to be a simple and suitable approach for achieving rechargeable batteries, due to the favorable chemical composition, structure, and interactions schematized in Fig. S7 (ESI†). However, the preliminary results indicate the need for further improvement to lower the polarization, increase the delivered capacity and enhance the cycle life, such as the change of the salt attempted in Fig. S8 (ESI†).

We thank JSPS KAKENHI 22KK0069, Ferrara University FAR2023, Dr Y. Goi (DKS Co. Ltd, Japan) for TOCNF hydrogel, Prof. Y. Nagatsu, Dr R. X. Suzuki (TUAT), Mr M. Takano (TA Instruments) for rheometer test.

Data availability

The data supporting this article have been included as part of the ESI.†

Conflicts of interest

There are no conflicts to declare.

References

1 M. Song, H. Tan, D. Chao and H. J. Fan, *Adv. Funct. Mater.*, 2018, **10**, 1802564.
2 L. E. Blanc, D. Kundu and L. F. Nazar, *Joule*, 2020, **4**, 771–799.
3 J. Shin and J. W. Choi, *Adv. Energy Mater.*, 2020, **28**, 2001386.
4 K. Kordesch and W. Taucher-Mautner, *Encyclopedia of Electrochemical Power Sources*, Elsevier, 2009, pp. 43–54.
5 J. Ming, J. Guo, C. Xia, W. Wang and H. N. Alshareef, *Mater. Sci. Eng.*, 2019, **135**, 58–84.
6 W. Liu, X. Zhang, Y. Huang, B. Jiang, Z. Chang, C. Xu and F. Kang, *J. Energy Chem.*, 2021, **56**, 365–373.
7 Z. Wang, H. Li, Z. Tang, Z. Liu, Z. Ruan, L. Ma, Q. Yang, D. Wang and C. Zhi, *Adv. Funct. Mater.*, 2018, **28**, 1804560.
8 K. Lu, T. Jiang, H. Hu and M. Wu, *Front. Chem.*, 2020, **8**, 546728.
9 Y. Tian, S. Chen, S. Ding, Q. Chen and J. Zhang, *Chem. Sci.*, 2023, **14**, 331–337.
10 T. Saito, Y. Nishiyama, J.-L. Putaux, M. Vignon and A. Isogai, *Biomacromolecules*, 2006, **7**, 1687–1691.
11 T. Saito, S. Kimura, Y. Nishiyama and A. Isogai, *Biomacromolecules*, 2007, **8**, 2485–2491.
12 A. Isogai, T. Saito and H. Fukuzumi, *Nanoscale*, 2011, **3**, 71–85.
13 B. Boukamp, *Solid State Ionics*, 1986, **20**, 31–44.
14 B. Boukamp, *Solid State Ionics*, 1986, **18–19**, 136–140.
15 Y. Sun, H. Ma, X. Zhang, B. Liu, L. Liu, X. Zhang, J. Feng, Q. Zhang, Y. Ding, B. Yang, L. Qu and X. Yan, *Adv. Funct. Mater.*, 2021, **31**, 2101277.
16 M. V. Nguyen, H. C. Dong, D. Nguyen-Manh, N. H. Vu, T. T. Trinh and T. B. Phan, *J. Sci.: Adv. Mater. Devices*, 2021, **6**, 509–515.
17 U. Fumio, Y. Hiroshi, N. Kumiko, N. Sachihiko, S. Kenji and M. Yasunori, *Int. J. Pharm.*, 1990, **58**, 135–142.
18 J.-B. Brubach, A. Mermet, A. Filabozzi, A. Gerschel and P. Roy, *J. Chem. Phys.*, 2002, **122**, 184509.
19 B. Abderrahim, E. Abderrahman, A. Mohamed, T. Fatima, T. Abdesselam and O. Krim, *World J. Environ. Eng.*, 2015, **3**, 95–110.
20 I. Ondrejkovičová, D. Mikloš and S. Štefániková, *Chem. Pap.*, 2008, **62**, 536–540.
21 V. Marangon, E. Barcaro, E. Scaduti, F. Adami, F. Bonaccorso, V. Pellegrini and J. Hassoun, *ACS Appl. Energy Mater.*, 2023, **6**, 11560–11572.
22 U. Ilyas, P. Lee, T. L. Tan, R. V. Ramanujan, S. Zhang, R. Chen, H. D. Sun and R. S. Rawat, *Int. J. Mod. Phys.: Conf. Ser.*, 2014, **32**, 1460341.
23 I. V. Pukhova, I. A. Kurzina, K. P. Savkin, O. A. Laput and E. M. Oks, *Nucl. Instrum. Methods Phys. Res., Sect. B*, 2017, **399**, 28–33.
24 T. Duguet, C. Bessaguet, M. Aufray, J. Esvan, C. Charvillat, C. Vahlas and C. Lacaze-Dufaure, *Appl. Surf. Sci.*, 2015, **324**, 605–611.
25 A. Morais, J. P. C. Alves, F. A. S. Lima, M. Lira-Cantu and A. F. Nogueira, *J. Photonics Energy*, 2015, **5**, 057408.
26 C. S. Kam, T. L. Leung, F. Liu, A. B. Djurišić, M. H. Xie, W.-K. Chan, Y. Zhou and K. Shih, *RSC Adv.*, 2018, **8**, 18355–18362.
27 R. Heinhold and M. W. Allen, *J. Mater. Res.*, 2012, **27**, 2214–2219.
28 Y. Sugano, M. Vestergaard, H. Yoshikawa, M. Saito and E. Tamiya, *Electroanalysis*, 2010, **22**, 1688–1694.
29 L. Li, T. K. A. Hoang, J. Zhi, M. Han, S. Li and P. Chen, *ACS Appl. Mater. Interfaces*, 2020, **12**, 12834–12846.
30 N. Zhang, F. Cheng, J. Liu, L. Wang, X. Long, X. Liu, F. Li and J. Chen, *Nat. Commun.*, 2017, **8**, 405.
31 W. Sun, F. Wang, S. Hou, C. Yang, X. Fan, Z. Ma, T. Gao, F. Han, R. Hu, M. Zhu and C. Wang, *J. Am. Chem. Soc.*, 2017, **139**, 9775–9778.
32 V. Marangon, E. Scaduti, V. F. Vinci and J. Hassoun, *ChemElectroChem*, 2022, **9**, e202200374.
33 Q. Li, X. Cui and Q. Pan, *ACS Appl. Mater. Interfaces*, 2019, **11**, 38762–38770.
34 S. Huang, S. He, Y. Li, S. Wang and X. Hou, *Chem. Eng. J.*, 2023, **464**, 142607.
35 L. Hong, X. Wu, Y. Liu, C. Yu, Y. Liu, K. Sun, C. Shen, W. Huang, Y. Zhou, J. Chen and K. Wang, *Adv. Funct. Mater.*, 2023, **33**, 2300952.
36 S. Wu, Z. Hu, P. He, L. Ren, J. Huangb and J. Luo, *eScience*, 2023, **3**, 100120.
37 K. Zhou, G. Liu, X. Zhu, G. Liu, X. Yu, Z. Guo and Y. Wang, *Angew. Chem., Int. Ed.*, 2024, e202413959, DOI: **10.1002/anie.202413959**.
38 K. Xie, K. Ren, Q. Wang, Y. Lin, F. Ma, C. Sun, Y. Li, X. Zhao and C. Lai, *eScience*, 2023, **3**, 100153.